The Journal of Clinical Investigation

AAV9-mediated FIG4 delivery prolongs life span in Charcot Marie Tooth disease type 4J mouse model.

Maximiliano Presa, … , Steven J. Gray, Cathleen Lutz

J Clin Invest. 2021. https://doi.org/10.1172/JCI137159.

Research In-Press Preview **Genetics** **Neuroscience**

Graphical abstract

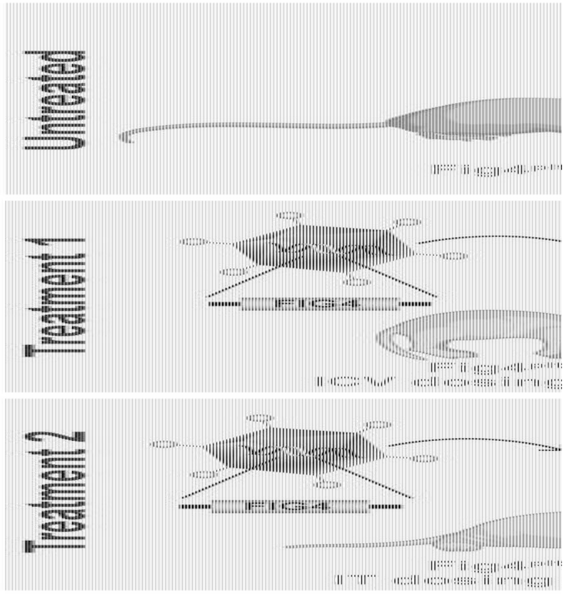

AAV9-mediated FIG4 delivery prolongs life span in Charcot Marie Tooth disease type 4J mouse model.

Maximiliano Presa[1], Rachel M Bailey[2], Crystal Davis[1], Tara Murphy[1], Jenn Cook[1], Randy Walls[1], Hannah Wilpan[1], Laurent Bogdanik[1], Guy M Lenk[3], Robert W Burgess[1], Steven J Gray[2], Cathleen Lutz[1]

Affiliations:

[1]The Jackson Laboratory, Bar Harbor, ME, USA.

[2]Department of Pediatrics, University of Texas Southwestern Medical Center, Dallas, TX, USA.

[3]Department of Human Genetics, University of Michigan, Ann Arbor, MI.

Conflict of interest: SJG and RMB are inventors on the *FIG4* vector design, and have received royalty income from Neurogene, LLC related to this invention. MP, CD, TM, JC, RW, HW, LB, GML, RWB and CL have declared that no conflict of interest exists.

Abstract

Charcot-Marie-Tooth disease type 4J (CMT4J) is caused by recessive, loss-of-function mutations in *FIG4*, encoding a phosphoinositol(3,5)P2-phosphatase. CMT4J patients have both neuron loss and demyelination in the peripheral nervous system, with vacuolization indicative of endosome/lysosome trafficking defects. Although the disease is highly variable, the onset is often in childhood and *FIG4* mutations can dramatically shorten lifespan. There is currently no treatment for CMT4J. Here we present the results of preclinical studies testing a gene therapy approach to restore *FIG4* expression. A mouse model of CMT4J, the *Fig4*-pale tremor (*plt*) allele, was dosed with a single-stranded AAV9 to deliver a codon-optimized human *FIG4* sequence. Untreated, $Fig4^{plt/plt}$ mice have a median survival of approximately 5 weeks. When treated with the AAV9-*FIG4* vector at postnatal day 1 or 4, mice survived at least one year, with largely normal gross motor performance and little sign of neuropathy by neurophysiological or histopathological evaluation. When treated at postnatal day 7 or 11, life span was still significantly prolonged and peripheral nerve function was improved, but rescue was less complete. No unanticipated adverse effects were observed. Therefore, AAV9-mediated delivery of *FIG4* is a well-tolerated and efficacious strategy in a mouse model of CMT4J.

Introduction:

Charcot-Marie-Tooth disease (CMT) is a collection of inherited motor and sensory neuropathies. Mutations in over eighty genes can lead to CMT, and it is highly heterogeneous(1). Loss of peripheral motor and sensory axon function through demyelination, axon degeneration, or a combination of these mechanisms is a disease hallmark(2).

Recessive mutations in *FIG4* underlie a rare form of the disease, CMT type 4J (CMT4J)(3). CMT4J usually involves the recurring I41T allele of *FIG4* in a compound heterozygous state with a truncating allele, such as a frame shift (3-5). CMT4J patients are highly variable in their presentation and severity, with cases ascertained from childhood through the sixth decade of life, though many present at the younger end of this spectrum. Nerve biopsy and neurophysiological examinations indicate axon loss, but also demyelination (3-5). Primary cells isolated from CMT4J patients show vacuoles that are LAMP2-positive, suggesting defects in endosome/lysosome trafficking (6). Mutations in *FIG4* also lead to other neurological and developmental disorders, depending on the severity of the loss-of-function caused by the mutations. Inheritance of two null alleles of *FIG4* leads to Yunis-Varon syndrome, which includes skeletal defects and severe neurological symptoms, with vacuolization and neuronal loss, typically resulting in death in infancy (7). Homozygosity for the D783V allele of *FIG4* results in bilateral temporooccipital polymicrogyria, which includes seizures (8). Thus, recessive mutations in *FIG4* lead to a variety of neurological conditions, which are generally severe and currently untreatable. Variants in *FIG4* have also been associated with adult onset amyotrophic lateral sclerosis and primary lateral sclerosis, although the pathogenicity of these alleles has not been firmly established (9).

The FIG4 protein is an phosphoinositol(3,5)P2-phosphatase. Importantly, it is in a complex with the enzymes that generate PI(3,5)P2, which are PIKFYVE and VAC14(10, 11). PI(3,5)P2 levels are very dynamic and important for multivesicular body formation and endosome/lysosome trafficking. Loss of FIG4 destabilizes this complex, resulting in the mislocalization of all three proteins and a reduction of PI(3,5)P_2. Mutations in *VAC14* also cause neurological disease in both mice and humans (12, 13). Therefore, some of the *FIG4* phenotype may be due to other components of this complex, such as

VAC14. Consistent with this, *Fig4* mutations in mice can be partially rescued with a catalytically inactive *Fig4* transgene (C486S) that may serve to restore protein interactions with VAC14 and PIKFYVE (12). However, the phenotype is more effectively rescued by a wild type *Fig4* gene (14). Importantly, neuronal expression of *Fig4* also rescues myelination, suggesting a non-cell autonomous effect (15). No adverse effects from *Fig4* transgenic overexpression were observed. Taken together, these results indicate CMT4J/*FIG4* mutations are excellent candidates for gene therapy to restore *FIG4* expression in peripheral neurons.

In the present study, we have performed preclinical testing of an AAV9 vector to deliver a codon-optimized wild-type human *FIG4* gene to neuronal and non-neuronal cells in a mouse model of CMT4J. The pale tremor (*plt*) mouse carries a transposon insertion in intron 18 of the mouse *Fig4* gene, resulting in a loss-of-function allele. The cloning of this mouse mutation led to the identification of *FIG4* as a human disease gene underlying CMT4J (3). The mice have a very similar phenotype, with demyelination, loss of motor neurons, and vacuolization in many regions of the nervous system, leading to a median lifespan of ~35 days when experiments are performed in a C57BL/6.C3H F1 genetic background (either inbred background alone survives only a few days). Restoration of *FIG4* expression using the gene therapy vector promoted survival to over one year when mice were treated at birth or at postnatal day four, and significantly prolonged survival when given by intrathecal injection into the lumbar spinal cord at postnatal day seven. Gross motor performance, peripheral axon function, and histopathological phenotypes were all improved. Thus, AAV9-mediated delivery of *FIG4* is efficacious in a mouse model of CMT4J.

Results:

AAV9/FIG4 gene therapy improves survival of Fig4 deficient mice.

The *Fig4* deficient mouse, or pale tremor (*plt*) mouse, presents a severe phenotype characterized by reduced life span, small body size, tremors, peripheral neuropathy, loss of motor neurons and hydrocephalus. The cloning of the spontaneous *plt* mutation in mice led to the identification of *FIG4* as the gene causing CMT4J in humans (3). Therefore, we used the $Fig4^{plt}$ mice as a proof-of-concept preclinical model for a gene replacement therapy to treat CMT4J using an AAV9/*FIG*4 vector (Figure 1A). The vector is a single stranded AAV9 carrying a codon-optimized wild type human *FIG4* cDNA driven by a ubiquitously expressed chicken beta-actin promoter with a CMV enhancer. To first demonstrate efficacy of the virus and gene replacement strategy, mice were treated at post-natal day 1 (PND1) and 4 (PND4) with the highest feasible dose of AAV9/FIG4 (5.4×10^{11} vg) via intracerebroventricular injection (ICV) (Figure 1B). All mice were genotyped at birth (PND0) and randomized among the different experimental groups and injected blinded for genotype and treatment. All cohorts were monitored daily for survival and body weight. As was previously reported (3), $Fig4^{plt/plt}$ mice that were untreated or vehicle-treated had a short life span, with a median survival age of 23 days (Figure 1C). After treatment with AAV9/*FIG4*, 90 % of $Fig4^{plt/plt}$ mice injected at PND1 survived more than 12 months (Fig. 1C). Although $Fig4^{plt/plt}$ mice treated at PND1 did gain weight and grow, they still showed a significantly lower body weight throughout their lifespan when compared to $Fig4^{+/+}$ littermates (Figure 1D). Both $Fig4^{+/+}$ treated at PND1 with AAV9/*FIG4* and untreated wild-type mice had 100 % survival after a year (Fig. 1C), with no differences in growth (Figure 1D), suggesting the AAV9/*FIG4* vector was well-tolerated in control mice.

We tested treatment efficacy by injecting at various later time points to approximate post-onset treatments that may be necessary clinically: at PND4 via ICV, and at PND7 and PND11 via lumbar intrathecal (IT) injections. As indicated in Figure 1C, 65% of the mice injected at PND4 survived more than one year, and half of those that did not survive died on the same time-course as untreated mice, possibly indicating failed injections. PND4 *Fig4*$^{plt/plt}$ mice treated with AAV9/*FIG4* followed a similar trajectory of growth and weight gain as PND1-treated *Fig4*$^{plt/plt}$ mice (Figure 1D).

To test the efficacy of AAV9/*FIG4* at later ages with a more advanced disease, we treated *Fig4*$^{plt/plt}$ mice at PND7 and PND11. IT delivery of 1.35 x10^{12} vg at PND7 resulted in an increased life span with a median survival age of 90 days (Figure 1E), whereas mice injected IT with the same dose at PND11 had a lower benefit with a median survival age of 17 days, not significantly different from vehicle-treated *Fig4*$^{plt/plt}$ mice (Figure 1E). All mice injected IT at PND7 or PND11 did grow and gain weight, but this varied with injection-age, with PND7-treated mice showing larger effects than PND11-treated cohort (Figure 1F).

These results indicate that treatment with AAV9/*FIG4* is able to improve survival and growth of *Fig4*$^{plt/plt}$ mice. The success of the treatment was dependent on the age of injection, with greater benefit at early ages (PND1 and 4), although IT treatment at PND7 also significantly improved survival (PND7 treated vs untreated *Fig4*$^{plt/plt}$ mice, $p<0.0001$) and growth.

As these experiments used the maximum feasible dose and produced a benefit in *Fig4*$^{plt/plt}$ mice both by ICV and IT delivery, we next performed a dose response experiment to determine the minimum dose able to produce a significant benefit with respect to body weight and survival. Since post-onset treatment and IT delivery are likely to reflect translational applications in clinical trials, we performed the dose-response experiment in PND7 animals treated via IT delivery. Both 1:5 (2.7x10^{11} vg, treated vs untreated $p<0.0001$) and 1:10 dilutions (1.35x10^{11} vg, treated vs untreated $p<0.0001$) still significantly extended lifespan in *Fig4*$^{plt/plt}$ animals, while a 1:100 dilution (1.35x10^{10} vg, treated vs untreated $p = 0.3842$) was not effective (Figure 1G). Similar results were observed in body weight, with *Fig4*$^{plt/plt}$ mice injected at 1:10 and 1:100 dilution gaining less weight compared to 1:5 and the maximum dose of AAV9/*FIG4* (Figure 1H).

FIG4 levels are restored in CNS after treatment with AAV9/FIG4.

Although a truncated *Fig4* mRNA has been reported in *Fig4*$^{plt/plt}$ mice, there is a complete absence of FIG4 protein by western blot (3). We assessed the effectiveness of AAV9/*FIG4* to induce human *FIG4* expression and improve FIG4 protein levels in CNS tissues of treated mice. The western blot analysis of whole brain or spinal cord shows absence of FIG4 in untreated *Fig4*$^{plt/plt}$ mice (Figure 2A, lane 5), whereas in mice injected at PND1 or 4, FIG4 was detected at same or slightly higher levels than untreated *Fig4*$^{+/+}$ mice (Figure 2A and B). In mice treated at PND7 with undiluted AAV9/*FIG4*, FIG4 protein was restored to slightly lower levels than untreated *Fig4*$^{+/+}$ mice in both brain and spinal cord (Figure 2C). As anticipated, FIG4 protein levels were dose-dependent, with lower levels in brain and spinal cord when mice were injected with a 1:5 dilution of the maximum dose (Figure 2C); however, the low overall FIG4 levels still produced a significant improvement in survival of *Fig4*$^{plt/plt}$ mice (Figure 1G).

AAV9/FIG4 gene therapy rescues muscle strength, motor coordination and overall activity in Fig4$^{plt/plt}$ *mice.*

An important clinical feature of CMT4J patients is the gradual loss of motor and neuromuscular function. To assess the benefits of the treatment on muscle strength, AAV9/*FIG4*-treated *Fig4*$^{plt/plt}$ mice were tested for grip strength, rotarod and wheel running and compared to untreated *Fig4* wildtype littermate mice to determine what fraction of strength could be recovered with treatment. Since untreated *Fig4*$^{plt/plt}$ mice do not survive long enough for perform these tests, they were not included. Mice treated with AAV9/*FIG4* at PND1 or PND4 by ICV delivery performed indistinguishably from wildtype mice at 6 months-of-age, indicating full rescue of rotarod, grip strength, and wheel running performance (Supplemental figure 1A-F). Importantly, there were also no behavioral changes in treated *Fig4*$^{+/+}$ mice, supporting the safety of AAV9/*FIG4*. Dose-response experiments showed a good rescue of *Fig4*$^{plt/plt}$ mice treated IT with 1:5 diluted AAV9/*FIG4* (2.7×10^{11} vg). Thus, we also assessed behavioral outcomes in *Fig4*$^{plt/plt}$ mice treated by IT injection at PND7 with a lower dose of AAV9/FIG4 to test the capacity of the treatment to provide benefit in a post-symptomatic disease setting beyond the improvements in survival and growth already described (Figure 1E-F). Rotarod analysis at 35 days-of-age revealed that the treated *Fig4*$^{plt/plt}$ mice had a shorter latency to fall when compared to *Fig4* wild type mice (Figure

2D), indicating the presence of some motor coordination deficits. However, in assessment of muscle strength, *Fig4*$^{plt/plt}$ treated mice showed similar grip strength compared to wild type mice (Figure 2E). Overall activity assessed by spontaneous wheel running showed no differences between treated *Fig4*$^{plt/plt}$ and wild type controls, although a trend towards lower activity in *Fig4*$^{plt/plt}$ treated mice can be observed (Figure 2F).

Nerve conduction velocity is improved by AAV9/FIG4

Fig4$^{plt/plt}$ mice develop hypomyelination features and reduced nerve conduction velocity (NCV) and compound muscle action potential (CMAP) amplitudes (3). When *Fig4*$^{plt/plt}$ mice were treated by ICV-injection with AAV9/*FIG4* at PND1, NCV was indistinguishable when compared to untreated *Fig4*$^{+/+}$ mice at 6 months-of-age, while PND4-injected mice showed a significant decrease in NCV (Figure 3A). However, when the remainder of the ICV-treated cohort was assessed at one-year post-treatment, the AAV9/*FIG4*-treated mice showed NCV values indistinguishable from wild type controls (Figure 3B). When AAV9/*FIG4* was delivered by IT injection at PND7, NCVs at 35 days-of-age were reduced in treated *Fig4*$^{plt/plt}$ mice compared to wild type untreated controls (Figure 3C). Despite these differences in NCV outcomes, the CMAP amplitude in all treated *Fig4*$^{plt/plt}$ mice was similar to wild type controls (Figure 3A-C, right panels). Thus, the degree of rescue of nerve function depended on the age and route of dosing, with better outcomes observed in the mice treated at PND1 (Figure 3A, B).

Wide biodistribution upon intrathecal delivery of AAV9/FIG4.

We assessed the viral copy number of AAV9/*FIG4* in mice that were ICV-injected at PND1-4 (assessed six months post-injection) and in mice that were IT-injected at PND7 (assessed approximately 100-120 days post-injection). The AAV9/*FIG4* vector was detected at high levels across multiple tissues (Figure 3D). Copy number was decreased in the brain of mice treated by IT injection compared to ICV-treated mice, which is likely a consequence of the different route of injection.

CNS and PNS pathology is improved in Fig4$^{plt/plt}$ *AAV9/FIG4 treated mice.*

The *Fig4*$^{plt/plt}$ mice have an accumulation of autophagosomes in multiple areas of the brain (cortex, hippocampus, cerebellum and brain stem), the spinal cord and dorsal root ganglion, producing vacuolization in these tissues (3). We performed a histopathological analysis in *Fig4*$^{plt/plt}$ and *Fig4*$^{+/+}$ treated mice with and without AAV9/*FIG4* treatment. Untreated *Fig4*$^{plt/plt}$ mice show pronounced vacuolization in DRG, spinal cord and cerebral cortex at 23 days-of-age (Figure 4A, middle column). In contrast, six months after ICV delivery of AAV9/*FIG4* at PND1, the degree of vacuole accumulation in *Fig4*$^{plt/plt}$ mice was almost completely rescued in DRG, spinal cord and brain (Figure 4A). While the later delivery of AAV9/FIG4 by IT injection was generally less effective than the ICV delivery at PND1 or 4, *Fig4*$^{plt/plt}$ mice treated by IT-delivery at PND7 showed a similar reduction of vacuole accumulation in spinal cord and DRG (Figure 4A, right column), although the brain was less well rescued. No vacuoles were detected in *Fig4*$^{+/+}$ mice when untreated or treated by ICV injected with AAV9/*FIG4*, supporting the safety of the treatment (Figure 4A, left columns).

The histopathological analysis of sciatic nerves indicated that untreated *Fig4*$^{plt/plt}$ have an increased frequency of small caliber axons. The treatment with AAV9/FIG4 in *Fig4*$^{plt/plt}$ was able to produce an increase in the frequency of large caliber axons (Figure 4B, C), which can be associated to the improvements in NCV reported by electrophysiology analysis (Figure 3). The mice injected IT at PND7 with AAV9/*FIG4* still present a significantly elevated frequency of small caliber axons (Figure 4B, left panel).

AAV9/FIG4 gene therapy improves autophagosome pathology in CNS of Fig4$^{plt/plt}$ *mice*

The *Fig4*$^{plt/plt}$ mice show an accumulation of autophagosomes with increased levels of the autophagosome-marker SQSTM1 (p62), usually followed by increased number of reactive astrocytes(11) Western blot analysis in brain and spinal cord of *Fig4*$^{plt/plt}$ mice treated at PND7 by IT delivery revealed a reduction in the abundance of p62 in both brain and spinal cord tissue when AAV9/*FIG4* was injected at the maximum dose, but a significant p62 reduction was observed only in brain in mice treated with diluted virus (Figure 4D). The gliosis marker GFAP was significantly decreased in spinal cord of *Fig4*$^{plt/plt}$ mice treated at PND7 with the maximum dose of AAV9/*FIG4*;

however, the diluted virus did not produce a change (Figure 4E). Thus, the improvement in these cellular markers was dose-dependent, and *Fig4*$^{plt/plt}$ mice treated by IT injection with a lower dose showed less improvement. These findings demonstrate that the AAV9/*FIG4* is directly correcting histopathological features in relevant neuronal cells types in the brain and spinal cord (Figure 4A).

Histopathology analysis and safety of AAV9/FIG4 treatment

To evaluate the safety of AAV9/*FIG4* gene therapy treatment, we performed histopathological analysis of multiple tissues dissected at six or twelve months post treatment. The analysis at six months across multiple tissues in wild type mice treated with AAV9/*FIG4* at PND1 by ICV delivery and untreated mice showed no major pathology findings as a consequence of the treatment (Supplemental table 1). Most notable findings in liver were micro and macrovesicular lipidosis and glycogen accumulation. We hypothesize this may be a consequence of long-term exposure to a diet-gel rich in carbohydrates (DietGel® 76A). However, twelve months post-treatment, hepatocellular carcinomas (HCC) were found in *Fig4*$^{+/+}$ mice in both untreated and ICV-AAV9/*FIG4* treated groups, and also in some of the *Fig4*$^{plt/plt}$ ICV treated mice. As indicated in supplemental table 2, we found an increased incidence of HCC in ICV-treated *Fig4*$^{+/+}$ mice (Fisher's exact test p-value = 0.0152). Liver tumor masses were also identified in *Fig4*$^{plt/plt}$ ICV-treated mice (PND1 and PND4); however, their incidence was not significantly increased compared to untreated mice (Fisher's exact test p-value = 0.5962).

HCC has been previously reported in mice treated with AAV vectors using strong promoters. Much of the tumorigenesis is attributed to integration of the vectors at the *Rian* locus, a rodent-specific sequence (16). To assess the possible integration of AAV9/*FIG4* in the mouse genome and whether the tumorigenic activity was related to insertion at the *Rian* locus as previously reported, one liver-solid mass was dissected from each liver sample, and whole genome sequencing was performed. The sequencing analysis detected unique integration events of the viral vector in multiple genomic regions (Supplemental figure 2A), with the *Rian* locus having the highest number of insertions. In 80 % of all HCC analyzed, it was possible to identify integrations at the *Rian* locus (p-value = 0.02) (Supplemental figure 2B). An elevated number of unique insertion events was also mapped to two genes, *Cps1* and the *Atrn-UTR3* (Supplemental figure 2A); however, these events were not associated with HCC samples (Supplemental figure 2C-D). All vector integrations identified at the *Rian* locus included the ITR and promoter regions of AAV9/*FIG4*.

We also performed a clinical blood chemistry analysis in untreated *Fig4*$^{plt/plt}$ mice at 23 days old, and AAV9/*FIG4* treated mice at 2, 7 and 12 months of age (Supplemental figure 3). No significant differences were observed between AAV9/*FIG4* treated and untreated cohorts for electrolytes (Na^+, K^+, Cl^-), glucose, creatinine, cholesterol, triglycerides (results not shown). However, liver enzymes were elevated in plasma of untreated *Fig4*$^{plt/plt}$ mice (Supplemental figure 3). A noticeable decrease in liver enzymes was observed in both ICV- and IT-treated mice at 2-8 months. However, ICV-treated mice at the 12-13 month end-point showed a significant increase in liver enzymes, and particularly the treated *Fig4*$^{+/+}$ mice, which is likely a consequence of the hepatic carcinomas detected in several of these mice (supplemental figure 3, central panel).

Discussion:

Our studies demonstrate the efficacy and tolerability of AAV9-delivered *FIG4* as a gene therapy treatment for CMT4J. The pale tremor mouse (*plt*) is a valid disease model for CMT4J, although perhaps more analogous to the more severe clinical designation of Yunis-Varon syndrome rather than the relatively more mild designation of CMT4J. Indeed, the identification of *Fig4* as the mutated gene in *plt* mice led to the identification of *FIG4* as the gene underlying CMT4J. Previous genetic studies in the *plt* mice established that the mutation is a recessive loss of function, and that restoring *Fig4* in the nervous system by transgenic expression was largely sufficient to rescue the phenotype (15). Our gene therapy strategy used AAV9 delivery of a codon-optimized human *FIG4* gene to accomplish much the same thing in a translationally relevant manner. Delivery of this vector at PND1 or 4 extended the life span of the *plt* mice from a few weeks to at least a year. Those mice had nearly normal behavioral, neurophysiological and histopathological phenotypes, though they were still smaller than wild type mice. Delaying treatment to PND 7 or 11 still provided benefit, but the rescue was less complete than at the earlier time points. The improvement we observed in nerve conduction in peripheral motor axons and the reduced vacuolization in the ventral spinal cord and dorsal root ganglia indicate that the vector is directly targeting cell populations clinically relevant to CMT4J. The only adverse effect noted, the development of hepatocellular carcinomas, is anticipated from the literature (16-19), and we confirmed that the incidence of these tumors can be explained by a peculiarity of the neonatal mouse genome. Thus, our results provide strong preclinical support for pursuing an AAV9-mediated gene replacement strategy with *FIG4* as a treatment for CMT4J.

In human genetic studies, CMT4J is consistent with straightforward, recessive loss-of-function alleles of *FIG4*. Typically, CMT4J patients are compound heterozygous for a presumed null allele (such as a frame shift or premature stop codon) and a nonsynonymous variant, most frequently the I41T substitution(5). The *plt* mouse harbors a null allele of *Fig4*, and thus, likely represents a more severe genetic perturbation than most CMT4J patients. Consistent with this, the mice have an aggressive, early onset phenotype, and show vacuolization in not just lower motor neurons, but also in sensory neurons and in various regions of the brain. Delivery of the AAV9/*FIG4* vector directly to the nervous system by ICV delivery was able to largely prevent these phenotypes, even rescuing the pathophysiology of neuronal populations in the brain that may not be directly affected in CMT4J patients. Conversely, CMT4J patients and the *plt* mice have signs of demyelinating neuropathy, and the Schwann cell-specific deletion of Fig4 in mice results in a phenotype, though not as severe as the ubiquitous deletion, suggesting *FIG4* expression is required in Schwann cells as well (5). However, in peripheral nerves of mice treated with AAV9/*FIG4* at PND1 or PND7, the g-ratio (axon diameter:total fiber diameter) was not different than wild-type control mice, suggesting that any peripheral myelination defects were corrected by treatment (supplemental figure 4A). Furthermore, mice treated by ICV delivery at PND1 had normal nerve conduction velocities, normal motor performance, and normal nerve histology. To assess if these benefits were from transduction of neurons or Schwann cells, we used in situ hybridization to detect *huFIG4* expression in combination with Schwann cell and motor neuron markers (supplemental figure 4B). In the sciatic nerve, 2% of all cells (DAPI nuclei) were transduced, and 7% of *Pmp22*-positive Schwann cells were also *huFIG4* positive. In contrast, in spinal cord sections, ~80% of *Chat*-positive motor neurons in the ventral horn were also *huFIG4*-positive. Previous transgenic mouse studies indicate that neuronal expression of *Fig4* was sufficient to rescue many aspects of the phenotype, including demyelination, suggesting a non-cell autonomous role for *FIG4(15)*. Our results using AAV9 are consistent with this interpretation, and the effects with this vector were profound when delivered at early postnatal ages. The low level of transduction in Schwann cells may account for some of the benefit observed, but presently, vectors and dosing regimens that efficiently transduce Schwann cells are not well-established. In contrast, given the high efficiency transduction of neurons we observed, we feel this accounts for most of the prolonged survival and improved motor performance and motor neuron physiology in the *plt* mice.

Our best rescue of the *plt*/CMT4J phenotype was obtained by treating as early as possible, at PND1. We faced two experimental limitations in this regard. First, the *plt* mice have an early and aggressive phenotype, reducing the feasibility of true post-onset trials in this mouse model. In addition, given the size of the *FIG4* gene and promoter sequences, we were restricted to using a single stranded AAV9 that is likely to take weeks to achieve full expression levels in transduced cells (20-22). With this in mind, it is likely a combination of factors that contribute to later treatment being less effective at PND7 or PND11: 1) increased degenerative disease state with irreversible damage, 2) expression that may be too slow to overcome the aggressive phenotype, and 3) decreased brain vector biodistribution in IT PND7/11 injections versus PND1/4 injections. Extrapolating these mouse time points to patients is challenging. Patients are likely to provide a window of treatment from months to years, not days, but we still fully anticipate that the earlier treatment can be provided, the greater the anticipated benefit. Our findings of reduced vacuolization in the DRG provide a hopeful result. This phenotype is evident even at perinatal time points(3), and the fact it is largely rescued with postnatal delivery of a single stranded AAV9 vector suggests there may be reversal of this cellular pathology, not just prevention or arrested progression. While AAV9-mediated replacement of *FIG4* is clearly not going to restore lost neurons, this result in mouse DRGs does suggest it may be able to reverse some hallmarks of neuronal dysfunction. The route of delivery is also a consideration. Our results suggest that transduction of neurons was responsible for the bulk of the benefit observed, supporting a targeted delivery to the CNS such as intrathecal injection. In addition, IT delivery has practical benefits such as smaller doses and thus smaller scale vector production and incurs less exposure of other tissues such as the liver and heart that are efficiently transduced by AAV9 when delivered systemically (23, 24).

The appearance of hepatocellular carcinomas (HCC) with delivery of AAV9/*FIG4* is not unanticipated based on literature, and we confirmed that our findings are consistent with these previous reports(16, 17, 19). In the neonatal mouse genome, AAV9 vectors are prone to integration in the *Rian* locus(16). Most of the integrations at *Rian* targets a microRNA, *Mir341.* Only the integration of strong promoter sequences in this location was reported to upregulate the expression of neighboring genes that may contribute to the tumorogenecity of these events(16). Integrations in *Rian* were the most abundant genomic abnormality found in HCCs analyzed after AAV9 transduction in our study, and in previous analyses (16, 18). Interestingly, the frequency of HCC in mice goes down rapidly with AAV9 transduction at older ages, suggesting the neonatal genome is more prone to these integrations, probably due to chromatin structure. Also, the *Rian* locus is not conserved in non-rodent species, and HCC has not been reported as a toxicological complication in AAV9 studies in humans or non-human primates. Given that we found HCC in 10/15 of our AAV9/*FIG4* treated mice, and 2/9 of our untreated mice at a year-of-age, and that we found integrations of the AAV9 vector and promoter sequence at the *Rian* locus in 8/10 of the treated tumor samples, we feel that the incidence of HCC in these mice can be accounted for by the proclivity of AAV9 vectors with strong promoters to integrate at the *Rian* locus in neonatal mice and promote tumor formation.

There is currently no treatment for CMT4J. The biology of PI(3,5)P2 is well studied, but also very complicated. It is not immediately obvious how one would design a pharmacological strategy to treat this disease. In addition, since *FIG4* is in a complex with the kinase PIKFYVE, PI(3,5)P2 levels are lower in the *plt* mice in contrast to what one might expect from the loss of the phosphatase. In contrast, the genetics of CMT4J seem to be relatively simple, with recessive loss-of-function mutations causing disease, although there are still some unresolved issues regarding cell-autonomy and the variability of clinical severity despite the apparent consistency of genotypes (5). The latter may be due to more complex genetic background effects, which are suggested by the mouse model as well. However, our preclinical studies with AAV9 delivery of *FIG4* were largely successful. It is worth exploring whether this approach could be further optimized, by also transducing Schwann cells, for example, but considering the often severe and debilitating symptoms of CMT4J patients and the lack of other treatment options, our results indicate that this gene therapy approach warrants further investigation.

Methods:

Animals and treatments:

Fig4 deficient mice carrying the pale tremor allele (*plt*) are maintained under specific pathogen free conditions at The Jackson Laboratory. Mice homozygous for the *plt* allele are neonatal lethal on a C57BL/6J background (B6.Cg-*Fig4*^{plt1}/MmJ, Stock N°: 17800) and they can survive up to two weeks on a C3HeB/FeJ background (C3Fe.Cg-*Fig4*^{plt1}/MmJ, Stock N°: 17801). However, in an F1 hybrid background, B6;C3H mice homozygous for the *plt* allele can survive 3-4 weeks (25). In this study, homozygous mice for the *plt* allele were generated by crossing heterozygous mice of both congenic stocks, generating an F1 hybrid B6;C3Fe-*Fig4*^{plt1}/MmJ. For efficacy and safety testing, 10 to 18, males and females mice homozygous *Fig4*$^{plt/plt}$ and wild type littermates *Fig4*$^{+/+}$ were randomly assigned to treatment groups at post-natal day 1 (PND1) or PND4 and dosed by intracerebroventricular (ICV) injection with 2 µl of either AAV9/FIG4 vector (5.4x10^{11} vg), or vehicle, or left untreated. For post-symptomatic efficacy testing, 10 to 14 male and female mice homozygous *Fig4*$^{plt/plt}$ were treated at PND7 or PND11 by intrathecal injection (IT) with 5 µl of either AAV9/FIG4 vector (13.5x10^{11} vg), or vehicle, or left untreated. Lower dose IT injections where conducted with the same volume and vehicle composition. All injections were performed blinded for compound and genotype. All mice were monitored daily for body weight, body conditioning and survival. Mice were euthanized when a body weight loss greater than 15 % or a body conditioning score lower than 2 (on a scale 1 – 3) was detected.

AAV9/FIG4 production:

An adeno-associated virus serotype 9 (AAV9) vector was engineered to encode the codon-optimized human *FIG4* gene for expression of the active human FIG4 enzyme. Three plasmids were used for manufacturing the AAV9/*FIG4* vector: the packaging/helper plasmids pGSK2/9 and pXX6-80 (which provide the AAV and Adenoviral helper functions needed for AAV vector production in mammalian cell culture), and the vector plasmid (pTR-CBA-hFIG4opt-spA). The vector plasmid contains the new 2721 bp optimized DNA coding sequence (hFIG4opt; ATUM, Newark, CA) cloned between a 1612 bp chicken beta actin (CBA) promoter with a CMV enhancer and a 48 bp Synthetic polyadenylation (SpA) signal. The transgene expression cassette is flanked by WT AAV2 ITRs (Figure 1A). The viral vector was produced by a triple-transfection method in HEK293 cells at the University of North Carolina Vector Core, as described (26). The final vector solution was formulated in PBS containing 350 mM NaCl (final concentration) and 5% sorbitol.

Western blot:

Whole tissue lysates were prepared in RIPA buffer (Thermo Fisher Scientific) containing Halt Protease Inhibitor Cocktail (Thermo Fisher Scientific). Tissue was homogenized using FastPrep®Z tubes (MP Biomedicals). Total soluble protein content was quantified by DC protein assay (Bio-Rad) and adjusted to 4 mg/ml in RIPA buffer. Protein lysates were prepared for automated Western blot using the Simple Wes system following vendor protocol (ProteinSimple, San Jose, CA). Anti-FIG4/Sac3 (clone N202/7, Antibodies Incorporated) was used at a 1:50 dilution, anti-P62/SQSTM1 (clone ab56416, Abcam) was used at a 1:2000 dilution, and anti-GFAP (clone NB300-141, Novus Biologicals) was used at 1:2000 dilution. Anti-GAPDH (mouse monoclonal MAB5718, R&D Systems or rabbit polyclonal NB300-322, Novus Biologicals) were used as loading controls at a 1:5000 -1:10000 dilution. Chemiluminescent signal was captured, and the resulting intensities were analyzed using the Compass for Simple Western software package (ProteinSimple). The target protein peak area was normalized to the loading control peak area following ProteinSimple recommendations and standard guidelines (27, 28). The relative fold change (RFC) was calculated using *Fig4*$^{+/+}$ mice as reference.

Behavior assessments

Rotarod:

An Ugo-Basile accelerating rotarod model 47600 for mice is used for this test. Mice were acclimated to the testing room for 60 min. The test begins placing the mice on the rotating rod at 4 rpm which accelerates up to 40 rpm over the course of 300 s. Each mouse is subjected to three consecutive trials with a 45 s resting interval. The time in seconds when the mouse falls from the rod is recorded.

Grip strength:

A commercially available Grip strength meter (Bioseb) was used to measure forelimb grip strength and/or combined forelimb/hindlimb grasp strength. For all measurements, a wire grid coupled to a strain gauge which measures peak force [kg] was used. The mice were weighed and allowed to acclimate to the testing room for a minimum of 60 minutes before the test begins. For forepaw testing, mice are held by their tails and lowered towards the grid to allow for visual placing and for the mouse to grip the grid with their forepaws. The animal is firmly pulled horizontally away from the grid for 6 consecutive trials with a brief inter-trial rest period. The first three trials are fore paw grip only, while the last 3 will include all four paws. The force peak is normalized to mouse body weight.

Spontaneous wheel running:

Animals are singly housed in a new cage with a running wheel, with food and water ad libitum. Running wheels (Med Associates) which are equipped with a wireless transponder that records activity on the running wheels (rpm) in sync with a computer that timestamps events. The mice were left undisturbed during the testing period of three nights and 2 days. Data was evaluated for total distance traveled during each day time period.

Electrophysiology

Sciatic nerve conduction velocity (NCV) was previously described (29). It was determined by measuring differences in compound muscle action potential (CMAP) latency in the muscles of the hind paw following sciatic nerve stimulation at two points (hip and ankle, NCV = distance between stimuli/difference in latency [hip - ankle]). The presence of conduction block was also evaluated by measuring the integrated CMAP in response to distal and proximal stimulation, where conduction block results in a smaller response to proximal stimulation, which must propagate a longer distance. Briefly, mice were anesthetized with isoflurane (1.5 – 2 %) and placed on a thermostatically regulated heating pad to maintain normal body temperature. For recording, the active needle electrode was inserted in the center of the paw and a reference electrode was placed in the skin between the first and second digits. The distance between points of stimulation and the recorded latencies was used in the calculation of velocity.

Histopathology analysis

Half of the cohort treated at PND1, PND4 were euthanized at 6 months-of-age and brain, spinal cord, skeletal muscle, heart, liver, kidney, gonads, mesenteric and cervical lymph nodes were dissected. Tissues were sectioned in half, one section was flash frozen for protein and DNA extraction and a second section was fixed in 10% NBF for histopathological assessments. Fixed brain, heart, liver, kidney, lymph nodes and gonads were paraffin-embedded and 5 µm sections were stained with H&E. Lumbar spinal cord was de-calcified with Immunocal (StatLab, TX) overnight, spinal cord and dorsal root ganglions (DRG) were dissected. DRG were mounted in histogel (Thermo Fisher Scientific) for paraffin embedding, sectioning and H&E staining. Histopathology analysis was conducted blinded for genotype and treatment by a board-certified veterinary pathologist at The Jackson Laboratory.

For histology nerve analysis, sciatic nerve was dissected and fixed overnight at 4°C in EM fixative (2 % PFA, 2 % glutaraldehyde, 0.1 M cacodylate buffer pH=7.2). Tissue was embedded in plastic blocks and semi-thin sections (1 µm) were stained with toluidine blue. Slides were scanned at 40x magnification and digital images analyzed with ImageJ for axon area distribution.

AAV9/FIG4 ISH:

Analysis of AAV9/huFIG4 expression was conducted by ISH using RNAScope® probes (ACD, Biotechne) specific for huFIG4 (hFIG4-codon-No-XMm-C2, catalog number 870051-C2), Pmp22 (Probe - Mm-Pmp22, catalog number 816571) and Chat (Probe – Mm-Chat, catalog number 408731). Mice injected ICV with AAV9/huFIG4 or vehicle were euthanized at 4 weeks of age. Spinal cord and sciatic nerve were dissected and mounted longitudinally in OCT. Longitudinal cryosections of spinal cord and sciatic nerve were double stained for Pmp22/huFIG4 (sciatic nerve) and Chat/huFIG4 (spinal cord), following RNAScope™ protocols. Images were captured in a Zeiss AxioImager.Z2 and number of positive cells by ROI manually counted using ImageJ software.

AAV9/FIG4 Biodistribution:

For analysis of vector biodistribution, mice treated by ICV injection with AAV9/*FIG4* at PND1 or PND4 were euthanized at 6 months age, and mice and mice treated by IT injection were euthanized at 3 months age. Genomic DNA was extracted from brain, spinal cord, liver, heart, muscle, kidney and gonads. Vector copy number was quantified by qPCR as previously described(24), using a specific set of primers for hFIG4opt (Forward: 5'-CGAGGACACCAACATGATCTAC-3', Reverse: 5'-CCACGTTCTGGAAGATTCTAAGG-3'), and Laminb2 (Forward: 5'-GGACCCAAGGACTACCTCAAGGG-3', Reverse: 5'- AGGGCACCTCCATCTCGGAAAC-3') to normalize and calculate the copies of viral genomes by µg of host DNA (vg/ µg).

HCC whole genome sequencing:

One tumor mass was dissected from each mouse liver, together with a liver sample visually free of tumor, and flash frozen. gDNA was extracted following standard methods. For library preparation 1 µg by sample of gDNA was used as input material. Sequencing libraries were generated using DNA Library Prep Kit (NEBNext®) following manufacturer's recommendations. The resulted libraries were fed into Illumina sequencers (HiSeqX, Illumina).

For sequence analysis, two tools, Virus-Clip (30) and BatVI (31), were used to detect possible integrations of the viral reference sequence pTR-CBA-hFIG4opt-spA. Both tools rely on using split-reads to determine possible integration sites. A split-read is identified when one portion of a sequencing read maps to one genomic location and another portion of the same sequencing read maps to a different genomic location. The tools return the number of split-reads supporting each proposed integration event. The total number of reads (sequencing depth) at each integration site, and the fraction of split-reads called by each tool at each integration site was calculated.

Statistics

Data were analyzed and graphed using Prism 7 software (GraphPad, San Diego, CA). Mann-Whitney t-test was used for comparisons between two groups. One-way or Two-way ANOVA test with Dunnett's correction was used for multiple group comparison. Statistical significance was set at $p<0.05$ for all comparisons.

Study approval

All animal treatments and procedures were approved by the Animal Care and Use Committee at The Jackson Laboratory.

Author contributions:

The AAV9/*FIG4* vector was designed and produced by RMB and SJG. Mouse studies and subsequent molecular analyses were performed by MP, CD, TM, JC, HW, and RW. Experimental design and interpretation were done by RWB, SJG and CL, with assistance from RMB, GML and MP. The manuscript was written by MP, RWB, SJG, and CL, with input from all authors.

Acknowledgments:

The authors are grateful for funding and support from the Cure CMT4J / Talia Duff Foundation (to SJG). This work was supported by The Center for Precision Genetics at The Jackson Laboratory (NIH grant U54 OD020351, U54 OD020351). The authors are grateful to the Scientific Services at The Jackson Laboratory for behavioral phenotyping, histology, and genome sequencing. These services are supported by NIH grant CA034196. RWB was supported by NIH R37 NS054154. GML was supported by NIGMS R01 GM24872. The authors are also grateful Jun Li (Wayne State University) for helpful discussions on the *Fig4*$^{\mathrm{plt}}$ mice and CMT4J clinical features, respectively.

References:

1. Timmerman V, Strickland AV, and Zuchner S. Genetics of Charcot-Marie-Tooth (CMT) Disease within the Frame of the Human Genome Project Success. *Genes (Basel).* 2014;5(1):13-32.
2. Saporta MA, and Shy ME. Inherited peripheral neuropathies. *Neurol Clin.* 2013;31(2):597-619.
3. Chow CY, Zhang Y, Dowling JJ, Jin N, Adamska M, Shiga K, et al. Mutation of FIG4 causes neurodegeneration in the pale tremor mouse and patients with CMT4J. *Nature.* 2007;448(7149):68-72.
4. Nicholson G, Lenk GM, Reddel SW, Grant AE, Towne CF, Ferguson CJ, et al. Distinctive genetic and clinical features of CMT4J: a severe neuropathy caused by mutations in the PI(3,5)P_2 phosphatase FIG4. *Brain.* 2011;134(Pt 7):1959-71.
5. Hu B, McCollum M, Ravi V, Arpag S, Moiseev D, Castoro R, et al. Myelin abnormality in Charcot-Marie-Tooth type 4J recapitulates features of acquired demyelination. *Ann Neurol.* 2018;83(4):756-70.
6. Zhang X, Chow CY, Sahenk Z, Shy ME, Meisler MH, and Li J. Mutation of FIG4 causes a rapidly progressive, asymmetric neuronal degeneration. *Brain.* 2008;131(Pt 8):1990-2001.
7. Campeau PM, Lenk GM, Lu JT, Bae Y, Burrage L, Turnpenny P, et al. Yunis-Varon syndrome is caused by mutations in FIG4, encoding a phosphoinositide phosphatase. *Am J Hum Genet.* 2013;92(5):781-91.
8. Baulac S, Lenk GM, Dufresnois B, Ouled Amar Bencheikh B, Couarch P, Renard J, et al. Role of the phosphoinositide phosphatase FIG4 gene in familial epilepsy with polymicrogyria. *Neurology.* 2014;82(12):1068-75.
9. Chow CY, Landers JE, Bergren SK, Sapp PC, Grant AE, Jones JM, et al. Deleterious variants of FIG4, a phosphoinositide phosphatase, in patients with ALS. *Am J Hum Genet.* 2009;84(1):85-8.
10. Jin N, Chow CY, Liu L, Zolov SN, Bronson R, Davisson M, et al. VAC14 nucleates a protein complex essential for the acute interconversion of PI3P and PI(3,5)P(2) in yeast and mouse. *Embo J.* 2008;27(24):3221-34.
11. Lenk GM, Ferguson CJ, Chow CY, Jin N, Jones JM, Grant AE, et al. Pathogenic mechanism of the FIG4 mutation responsible for Charcot-Marie-Tooth disease CMT4J. *PLoS Genet.* 2011;7(6):e1002104.
12. Lenk GM, Szymanska K, Debska-Vielhaber G, Rydzanicz M, Walczak A, Bekiesinska-Figatowska M, et al. Biallelic Mutations of VAC14 in Pediatric-Onset Neurological Disease. *Am J Hum Genet.* 2016;99(1):188-94.
13. Zhang Y, Zolov SN, Chow CY, Slutsky SG, Richardson SC, Piper RC, et al. Loss of Vac14, a regulator of the signaling lipid phosphatidylinositol 3,5-bisphosphate, results in neurodegeneration in mice. *Proc Natl Acad Sci U S A.* 2007;104(44):17518-23.
14. Ferguson CJ, Lenk GM, Jones JM, Grant AE, Winters JJ, Dowling JJ, et al. Neuronal expression of Fig4 is both necessary and sufficient to prevent spongiform neurodegeneration. *Human molecular genetics.* 2012;21(16):3525-34.
15. Winters JJ, Ferguson CJ, Lenk GM, Giger-Mateeva VI, Shrager P, Meisler MH, et al. Congenital CNS hypomyelination in the Fig4 null mouse is rescued by neuronal expression of the PI(3,5)P(2) phosphatase Fig4. *J Neurosci.* 2011;31(48):17736-51.
16. Chandler RJ, LaFave MC, Varshney GK, Trivedi NS, Carrillo-Carrasco N, Senac JS, et al. Vector design influences hepatic genotoxicity after adeno-associated virus gene therapy. *The Journal of Clinical Investigation.* 2015;125(2):870-80.
17. Colella P, Ronzitti G, and Mingozzi F. Emerging Issues in AAV-Mediated In Vivo Gene Therapy. *Molecular Therapy - Methods & Clinical Development.* 2018;8:87-104.
18. Donsante A, Miller DG, Li Y, Vogler C, Brunt EM, Russell DW, et al. AAV Vector Integration Sites in Mouse Hepatocellular Carcinoma. *Science.* 2007;317(5837):477-.
19. Ferla R, Alliegro M, Dell'Anno M, Nusco E, Cullen JM, Smith SN, et al. Low incidence of hepatocellular carcinoma in mice and cats treated with systemic adeno-associated viral vectors. *Molecular Therapy - Methods & Clinical Development.* 2021;20:247-57.
20. Gray SJ, Foti SB, Schwartz JW, Bachaboina L, Taylor-Blake B, Coleman J, et al. Optimizing promoters for recombinant adeno-associated virus-mediated gene expression in the peripheral and central nervous system using self-complementary vectors. *Hum Gene Ther.* 2011;22(9):1143-53.
21. Zincarelli C, Soltys S, Rengo G, and Rabinowitz JE. Analysis of AAV Serotypes 1–9 Mediated Gene Expression and Tropism in Mice After Systemic Injection. *Molecular Therapy.* 2008;16(6):1073-80.
22. Malik AK, Monahan PE, Allen DL, Chen BG, Samulski RJ, and Kurachi K. Kinetics of recombinant adeno-associated virus-mediated gene transfer. *J Virol.* 2000;74(8):3555-65.

23. Bailey RM, Rozenberg A, and Gray SJ. Comparison of high-dose intracisterna magna and lumbar puncture intrathecal delivery of AAV9 in mice to treat neuropathies. *Brain Res.* 2020;1739:146832.
24. Gray SJ, Matagne V, Bachaboina L, Yadav S, Ojeda SR, and Samulski RJ. Preclinical Differences of Intravascular AAV9 Delivery to Neurons and Glia: A Comparative Study of Adult Mice and Nonhuman Primates. *Molecular Therapy.* 2011;19(6):1058-69.
25. Lenk GM, and Meisler MH. In: Conn PM ed. *Methods in Enzymology*. Academic Press; 2014:245-60.
26. Grieger JC, Soltys SM, and Samulski RJ. Production of Recombinant Adeno-associated Virus Vectors Using Suspension HEK293 Cells and Continuous Harvest of Vector From the Culture Media for GMP FIX and FLT1 Clinical Vector. *Mol Ther.* 2016;24(2):287-97.
27. Taylor SC, and Posch A. The Design of a Quantitative Western Blot Experiment. *BioMed Research International.* 2014;2014:8.
28. Fosang AJ, and Colbran RJ. Transparency Is the Key to Quality. *Journal of Biological Chemistry.* 2015;290(50):29692-4.
29. Bogdanik LP, Sleigh JN, Tian C, Samuels ME, Bedard K, Seburn KL, et al. Loss of the E3 ubiquitin ligase LRSAM1 sensitizes peripheral axons to degeneration in a mouse model of Charcot-Marie-Tooth disease. *Disease Models &amp; Mechanisms.* 2013;6(3):780.
30. Ho DWH, Sze KMF, and Ng IOL. Virus-Clip: a fast and memory-efficient viral integration site detection tool at single-base resolution with annotation capability. *Oncotarget.* 2015;6(25):20959-63.
31. Tennakoon C, and Sung WK. BATVI: Fast, sensitive and accurate detection of virus integrations. *BMC Bioinformatics.* 2017;18(Suppl 3):71-.

Figure 1

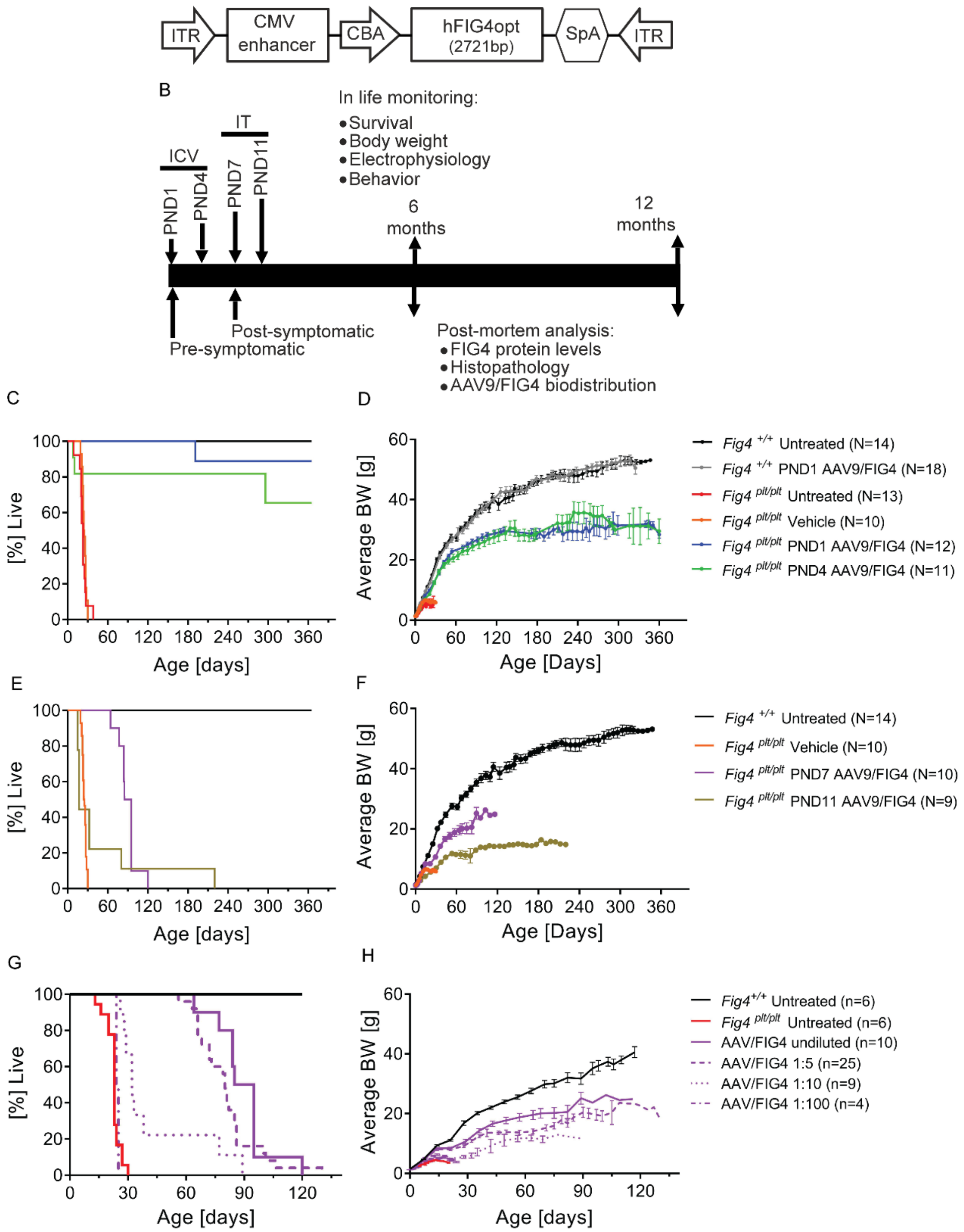

Figure 1: Neonatal delivery of AAV9/*FIG4* vector improves survival of *Fig4*$^{plt/plt}$ mice.
(A) Representation of the AAV9/*FIG4* vector, with a full-length, codon-optimized human *FIG4* cDNA (hFIG4opt) under control of the chicken beta actin (CBA) promoter, including a CMV-derived enhancer and a synthetic poly(A) tail (SpA). This expression cassette was flanked by an inverted terminal repeat (ITR) sequence for packing into AAV9. (B) Outline of preclinical study design. *Fig4*$^{plt/plt}$ mice were treated by ICV injection at post-natal day 1 (PND1) or 4 (PND4) with AAV9/*FIG4*, representing the "pre-symptomatic" intervention and proof-of-concept group for efficacy testing. *Fig4* wild type littermates were dosed ICV at PND1 representing the "safety" group for AAV9/*FIG4* toxicity evaluation. Both *Fig4*$^{plt/plt}$ and wild type mice treated with vehicle or untreated were included as controls. For post-symptomatic treatments, *Fig4*$^{plt/plt}$ were treated at PND7 or PND11 via intrathecal (IT) injection. A minimum N=5 mice per sex per genotype was enrolled in each group. All mice were monitored daily for body weight and survival. Electrophysiology and behavioral assessments were conducted at various time point after AAV9/*FIG4* treatment. Part of the ICV injected group were analyzed at 6-8 months post-treatment and the rest at the 12-13 months end point. (C) Survival and (D) average body weights for mice injected with AAV9/*FIG4* via ICV (5.4x10^{11} vg) at PND1 and PND4. For post-symptomatic intervention, *Fig4*$^{plt/plt}$ mice were treated by IT injection (AAV9/*FIG4*, 1.35 x10^{12} vg) at PND7 and PND11, (E) Survival and (F) average body weights are shown. Dose-response analysis was conducted by injecting *Fig4*$^{plt/plt}$ mice via IT with AAV9/*FIG4* diluted 1:5 (2.7x10^{11} vg), 1:10 (1.35x10^{11} vg) and 1:100 (1.35x10^{10} vg). (G) Survival and (H) average body weights are shown. Log-rank (Mantel-Cox) test was applied for survival curve comparisons. Growth curves are average body weight ± SEM.

Figure 2

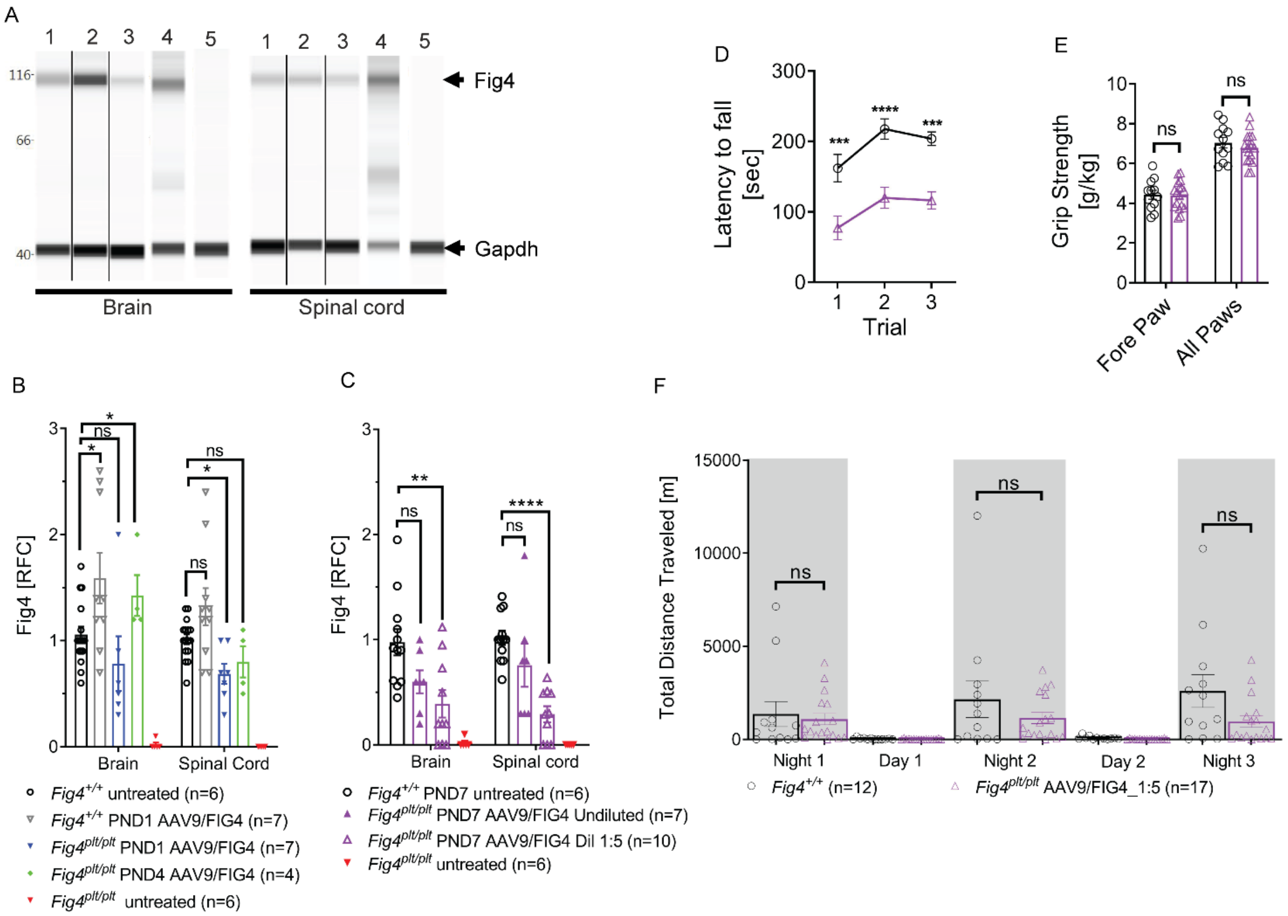

Figure 2: AAV9/*FIG4* therapy restore FIG4 protein levels and behavioral outcomes of *Fig4*$^{plt/plt}$ mice.
FIG4 protein levels were assessed in whole protein lysates from brain and spinal cord by western blot. Mice treated at PND1 or 4 by ICV injection of the maximum AAV9/FIG4 dose were analyzed at 6 months-of-age. A) Representative western blot showing detection of FIG4 as a single band at 112 kDa, present in *Fig4*$^{+/+}$ untreated mice (lane 1), *Fig4*$^{+/+}$ treated at PND1 (lane 2), *Fig4*$^{plt/plt}$ treated at PND1 (lane 3), *Fig4*$^{plt/plt}$ treated at PND4 treated (lane 4), and not present in *Fig4*$^{plt/plt}$ untreated mice (lane 5). B) The FIG4 levels were normalized to GAPDH as a loading control, and relative fold change (RFC) calculated using *Fig4*$^{+/+}$ untreated mice as reference. C) The average RFC 100-120 days-of-age for IT treated mice at PND7 with maximum or 1:5 diluted AAV9/*FIG4*. D-F) *Fig4*$^{plt/plt}$ mice treated by IT delivery at PND7 with AAV9/*FIG4* (1:5 dilution, 2.7x10^{11} vg) were assessed 35 days post-treatment for motor coordination performance, grip strength and general activity. (D) Rotarod analysis is reported as the latency to fall during three trials. (E) Average grip strength normalized to body weight in the fore paws and all paws is shown. (F) General activity was assessed by monitoring voluntary wheel running, the average total distance traveled at each day time cycle is reported. Data represents the average ±SEM of combined males and females, since no significant differences were observed by sex. Groups were compared by two-way ANOVA with Dunnett's correction for multiple comparisons (B, C) and Mann-Whitney t-test (D-F), ns = not significant, p>0.05, * p<0.05, ** p<0.01, *** p<0.001, **** p<0.0001.

Figure 3

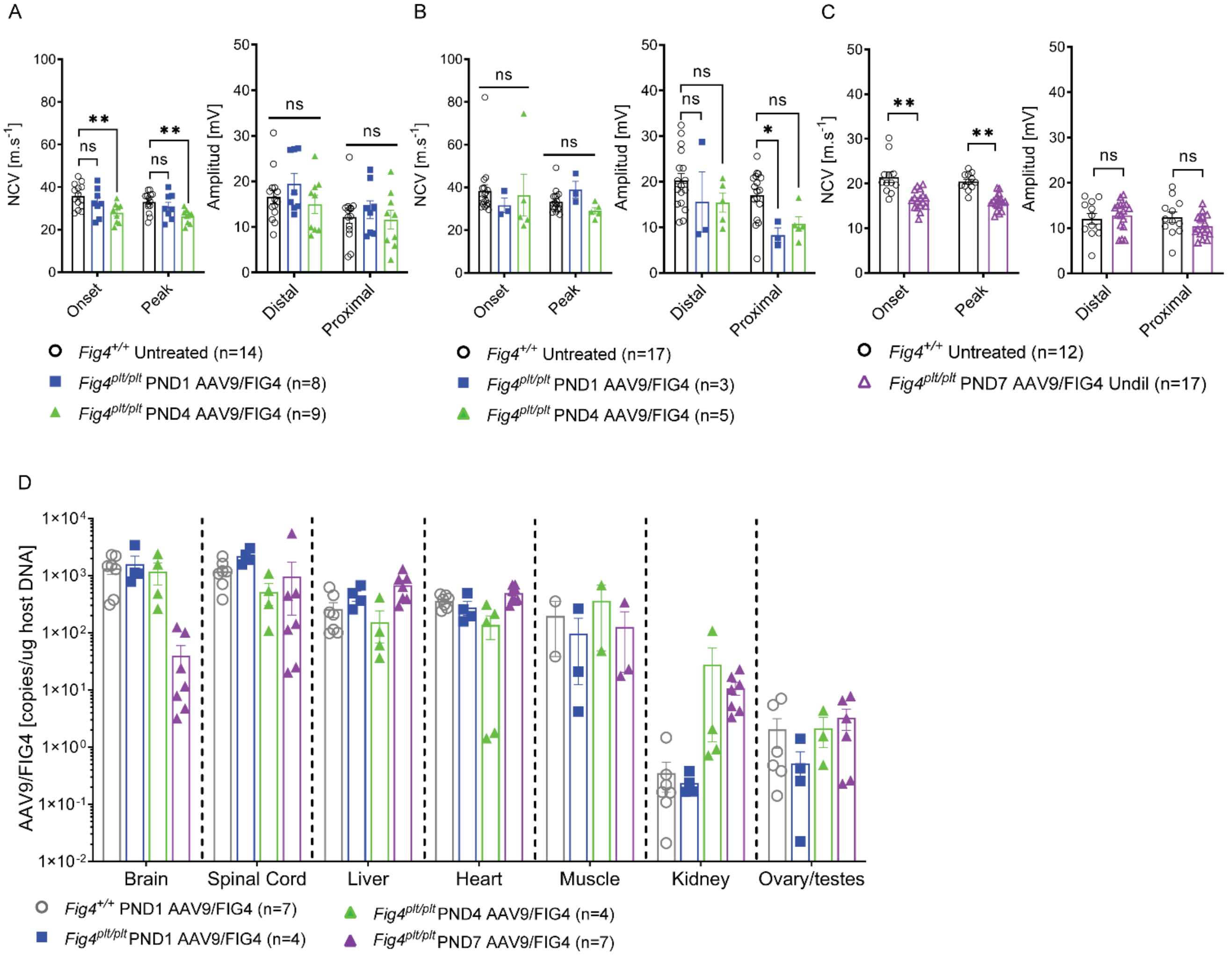

Figure 3: AAV9/*FIG4* treatment provide a wide biodistribution and improve NCV outcomes in an age of injection and dose dependent manner.
Sciatic nerve conduction velocity of motor axons and CMAP was assessed at six months (A) and 12 months (B) post- ICV treatment of *Fig4*$^{plt/plt}$ mice and wild type controls. *Fig4*$^{plt/plt}$ mice IT-injected with AAV9/*FIG4* 1:5 dilution (2.7x10^{11} vg) were assessed at 35 days post-treatment (C). Tissues were collected from mice treated with AAV9/*FIG4* at six months (ICV treatment) and four months (IT treatment) post treatment. The vector copy number was assessed by quantitative PCR as copies/µg of genomic DNA. (D). Data represent the average ±SEM of combined males and females, since no significant differences were observed by sex. Groups were compared by two-way ANOVA with correction for multiple comparisons using Dunnett's test (A, B) or Bonferroni test (C), ns = not significant, p>0.05, * p<0.05, ** p<0.01.

Figure 4

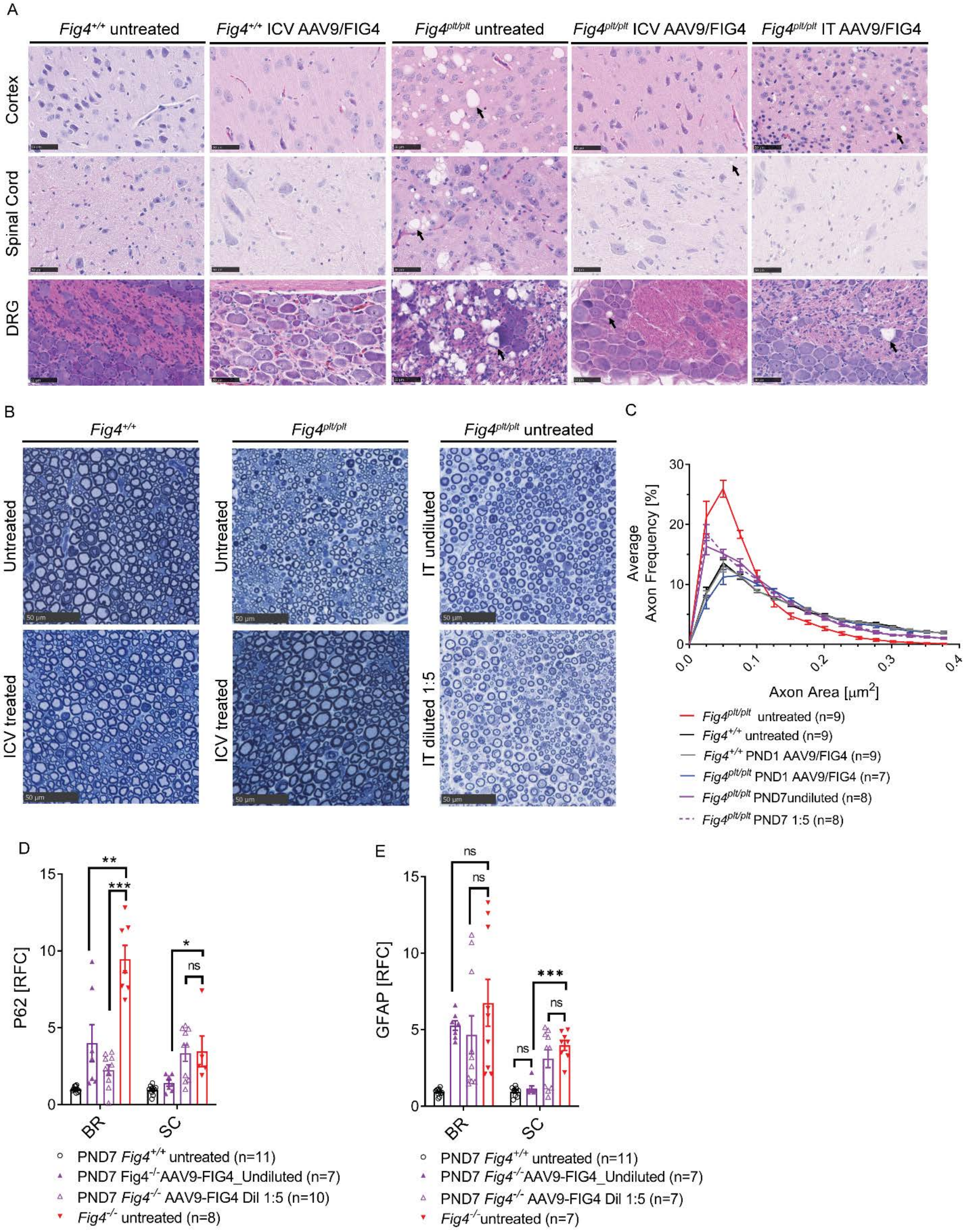

Figure 4: CNS pathology is reduced in AAV9/*FIG4*-treated *Fig4$^{plt/plt}$* mice

Histopathology changes were assessed in ICV, IT AAV9/FIG4 treated and untreated *Fig4$^{plt/plt}$* mice and wild type controls. (A) Representative H/E images of motor cortex, thoracic spinal cord (ventral horn) and dorsal root ganglions (DRG) dissected from the indicated groups, scale bar = 50 µm. Black arrows indicate cytoplasmic vacuoles. (B) Representative semi-thin sections of toluidine-blue stained sciatic nerve were analyzed for axon size distribution. Cross-sections of sciatic nerve were scanned at 40x and axon caliber for each axon in the section was determined using ImageJ software (C) Distribution of the Average axon frequency by size (axon area 50 µm). The autophagosome marker SQSTM1 (p62) and the astrocyte marker GFAP were analyzed by quantitative western blot in protein lysates of brain (BR) and spinal cord (SC). p62 and GFAP signal was normalized to GAPDH loading control. Relative fold change (RFC) was calculated using *Fig4$^{+/+}$* untreated tissue as reference. *Fig4$^{plt/plt}$*–derived protein extracts were prepared from 23 days old untreated mice. Bars represent the average ±SEM. Statistical significance was calculated by one-way ANOVA with Dunnett test correction for multiple comparisons, ns = not significant, p>0.05, * p<0.05, ** p<0.01, *** p<0.001.